Qiang, X., Zhou, X., Wang, J., Wilkes, C., Loke, T., O'Gara, S., ... Matthews, J. (2018). Large-scale silicon quantum photonics implementing arbitrary two-qubit processing. *Nature Photonics*, *12*(9), 534-539. https://doi.org/10.1038/s41566-018-0236-y

Supplementary Information for: Large-scale silicon quantum photonics implementing arbitrary two-qubit processing

Xiaogang Qiang,[1,3,4] Xiaoqi Zhou,[2,1,*] Jianwei Wang,[1] Callum M. Wilkes,[1] Thomas Loke,[5] Sean O'Gara,[1] Laurent Kling,[1] Graham D. Marshall,[1] Raffaele Santagati,[1] Jingbo B. Wang,[5] Timothy C. Ralph,[6] Jeremy L. O'Brien,[1] Mark G. Thompson,[1] and Jonathan C. F. Matthews[1,†]

[1] *Quantum Engineering Technology Labs, H. H. Wills Physics Laboratory and Department of Electrical & Electronic Engineering, University of Bristol, BS8 1FD,UK.*
[2] *State Key Laboratory of Optoelectronic Materials and Technologies and School of Physics, Sun Yat-sen University, Guangzhou 510275, China*
[3] *State Key Laboratory of High Performance Computing and School of Computer Science, NUDT, Changsha 410073, China*
[4] *National Innovation Institute of Defense Technology, AMS, Beijing 100071, China*
[5] *School of Physics, The University of Western Australia, Crawley WA 6009, Australia*
[6] *Centre for Quantum Computation and Communication Technology, Department of Mathematical and Physics, The University of Queensland, St. Lucia, Queensland 4072, Australia*

(Dated: April 15, 2018)

I. LINEAR-COMBINATION SCHEME FOR UNIVERSAL TWO-QUBIT UNITARY OPERATION

A. Probabilistic circuit for linear-combination of quantum gates

Here we present more details of the circuit shown in Fig. 1(B) in the main text that is the design to implement the general linear combination of quantum gates probabilistically. It stands for general dimensionality spaces. U_{LC} in the circuit is a unitary operation defined as

$$U_{\mathrm{LC}} = \begin{pmatrix} \alpha_0 & \alpha_1 & \cdots & \alpha_{n-1} \\ u_{2,1} & u_{2,2} & \cdots & u_{2,n-1} \\ \vdots & \vdots & \ddots & \vdots \\ u_{n-1,1} & u_{n-1,2} & \cdots & u_{n-1,n-1} \end{pmatrix}, \tag{S1}$$

whose first row decides the linear coefficients α_i. The circuit evolves as below:

$$\overbrace{|00\cdots0\rangle}^{k}|\varphi\rangle \tag{S2}$$

$$\rightarrow \frac{1}{2^{k/2}}\left(\overbrace{|00\cdots0\rangle}^{k}|\varphi\rangle + \overbrace{|00\cdots1\rangle}^{k}|\varphi\rangle + \cdots + \overbrace{|11\cdots1\rangle}^{k}|\varphi\rangle\right) \tag{S3}$$

$$\rightarrow \frac{1}{2^{k/2}}\left(\overbrace{|00\cdots0\rangle}^{k}V_0|\varphi\rangle + \overbrace{|00\cdots1\rangle}^{k}V_1|\varphi\rangle + \cdots + \overbrace{|11\cdots1\rangle}^{k}V_{n-1}|\varphi\rangle\right) \tag{S4}$$

$$\rightarrow \frac{1}{2^{k/2}}\left[\left(\alpha_0\overbrace{|00\cdots0\rangle}^{k} + u_{2,1}\overbrace{|00\cdots1\rangle}^{k} + \cdots + u_{n-1,1}\overbrace{|11\cdots1\rangle}^{k}\right)V_0|\varphi\rangle\right. \tag{S5}$$

$$+\left(\alpha_1\overbrace{|00\cdots0\rangle}^{k} + u_{2,2}\overbrace{|00\cdots1\rangle}^{k} + \cdots + u_{n-1,2}\overbrace{|11\cdots1\rangle}^{k}\right)V_1|\varphi\rangle \tag{S6}$$

$$\cdots \tag{S7}$$

$$\left.+\left(\alpha_{n-1}\overbrace{|00\cdots0\rangle}^{k} + u_{2,n-1}\overbrace{|00\cdots1\rangle}^{k} + \cdots + u_{n-1,n-1}\overbrace{|11\cdots1\rangle}^{k}\right)V_{n-1}|\varphi\rangle\right] \tag{S8}$$

$$\tag{S9}$$

$$\rightarrow \frac{1}{2^{k/2}} \left[\overbrace{|00\cdots0\rangle}^{k} \left(\sum_{i=0}^{n-1} \alpha_i V_i \right) |\varphi\rangle + \overbrace{|00\cdots1\rangle}^{k} \left(\sum_{i=0}^{n-1} u_{2,i} V_i \right) |\varphi\rangle + \cdots + \overbrace{|11\cdots1\rangle}^{k} \left(\sum_{i=0}^{n-1} u_{n-1,i} V_i \right) |\varphi\rangle \right] \tag{S10}$$

When all auxiliary qubits were measured to be "0" in the computational basis, the linear-combination operation $\sum_{i=0}^{n-1} \alpha_i V_i$ would be implemented. The success probability is $1/k$, where $k = 2^n$.

B. Linear-combination decomposition of SU(4)

By using the Cartan's KAK decomposition[1], an arbitrary two-qubit unitary operation $U \in \mathrm{SU}(4)$ can be decomposed as:

$$U = (P_1 \otimes P_2) U_{\mathrm{D}} (Q_1 \otimes Q_2), \tag{S11}$$

where P_1, P_2, Q_1 and Q_2 are single-qubit gates, and U_{D} represents the gate below:

$$U_{\mathrm{D}} = \exp(-i(k_1 \sigma_1 \otimes \sigma_1 + k_2 \sigma_2 \otimes \sigma_2 + k_3 \sigma_3 \otimes \sigma_3)). \tag{S12}$$

Here k_i $(i = 1, 2, 3)$ are real numbers, and σ_i are Pauli matrices σ_x, σ_y and σ_z. A step-by-step procedure of applying Cartan's KAK decomposition onto SU(4) can be found in ref 2.

Considering the fact that

$$\exp(iAx) = \cos(x) I + i \sin(x) A \tag{S13}$$

for an arbitrary real number x and a matrix A satisfying $A^2 = I$ (ref. 3), U_{D} can be reformed as:

$$U_{\mathrm{D}} = (\cos(k_1) I \otimes I - i \sin(k_1) \sigma_x \otimes \sigma_x) \cdot (\cos(k_2) I \otimes I - i \sin(k_2) \sigma_y \otimes \sigma_y) \cdot (\cos(k_3) I \otimes I - i \sin(k_3) \sigma_z \otimes \sigma_z) \tag{S14}$$

We also have the results that

$$\sigma_x \sigma_y = -\sigma_y \sigma_x = i \sigma_z, \tag{S15}$$
$$\sigma_y \sigma_z = -\sigma_z \sigma_y = i \sigma_x, \tag{S16}$$
$$\sigma_z \sigma_x = -\sigma_x \sigma_z = i \sigma_y. \tag{S17}$$

From Equations (S11), (S14) and (S15)-(S17), we can rewrite U into a linear-combination form:

$$U = \alpha_0 A_0 \otimes B_0 + \alpha_1 A_1 \otimes B_1 + \alpha_2 A_2 \otimes B_2 + \alpha_3 A_3 \otimes B_3 \tag{S18}$$

where α_0, α_1, α_2 and α_3 are four complex coefficients obtained from k_i:

$$\begin{aligned}
\alpha_0 &= (\cos(k_1)\cos(k_2)\cos(k_3) - i \sin(k_1)\sin(k_2)\sin(k_3)), \\
\alpha_1 &= (\cos(k_1)\sin(k_2)\sin(k_3) - i \sin(k_1)\cos(k_2)\cos(k_3)), \\
\alpha_2 &= (\sin(k_1)\cos(k_2)\sin(k_3) - i \cos(k_1)\sin(k_2)\cos(k_3)), \\
\alpha_3 &= (\sin(k_1)\sin(k_2)\cos(k_3) - i \cos(k_1)\cos(k_2)\sin(k_3)),
\end{aligned} \tag{S19}$$

and they satisfy $\sum_{i=0}^{3} |\alpha_i|^2 = 1$. It is easy to verify that A_i, B_i $(i = 0, \cdots, 3)$ are single-qubit operations as below:

$$\begin{aligned}
A_0 &= P_1 I Q_1, \quad & B_0 &= P_2 I Q_2, \\
A_1 &= P_1 \sigma_x Q_1, \quad & B_1 &= P_2 \sigma_x Q_2, \\
A_2 &= P_1 \sigma_y Q_1, \quad & B_2 &= P_2 \sigma_y Q_2, \\
A_3 &= P_1 \sigma_z Q_1, \quad & B_3 &= P_2 \sigma_z Q_2.
\end{aligned} \tag{S20}$$

It is an interesting open question that whether the procedure shown above can be directly applied to higher dimensionality spaces to obtain their corresponding linear-combination expressions.

C. Deterministic linear-combination circuit for universal two-qubit unitary gates

The proposed circuit shown in Fig. 1(C) in the main text can implement the linear combination of four tensor products of two single-qubit gates, i.e., the universal two-qubit unitary gate according to Equation (S18) deterministically. Here we show how it works in details. Suppose the four linear coefficients are α_0, α_1, α_2 and α_3, the required U_{LC} in the circuit is given by:

$$U_{\mathrm{LC}} = \begin{pmatrix} \alpha_0 & \alpha_1 & \alpha_2 & \alpha_3 \\ \alpha_1 & \alpha_0 & -\alpha_3 & -\alpha_2 \\ \alpha_2 & -\alpha_3 & \alpha_0 & -\alpha_1 \\ \alpha_3 & -\alpha_2 & -\alpha_1 & \alpha_0 \end{pmatrix} \tag{S21}$$

We first show that such a unitary U_{LC} always exists for an arbitrary $U \in \mathrm{SU}(4)$.

Proof. An arbitrary $U \in \mathrm{SU}(4)$ can be decomposed into the form

$$U = \sum_{i=0}^{3} \alpha_i \left(P_1 \sigma_i Q_1\right) \otimes \left(P_2 \sigma_i Q_2\right) = \left(P_1 \otimes P_2\right) \left(\sum_{i=0}^{3} \alpha_i \sigma_i \otimes \sigma_i\right) \left(Q_1 \otimes Q_2\right) \tag{S22}$$

(see Section I.A). U being unitary implies that its non-local part: $U_{\mathrm{D}} = \sum_{i=0}^{3} \alpha_i \sigma_i \otimes \sigma_i$ is unitary, i.e., $U_{\mathrm{D}} {U_{\mathrm{D}}}^{\dagger} = I \otimes I$. On the other hand,

$$\begin{aligned} UU^{\dagger} &= \left(\alpha_0 I \otimes I + \alpha_1 \sigma_x \otimes \sigma_x + \alpha_2 \sigma_y \otimes \sigma_y + \alpha_3 \sigma_z \otimes \sigma_z\right) \left({\alpha_0}^{\dagger} I \otimes I + {\alpha_1}^{\dagger} \sigma_x \otimes \sigma_x + {\alpha_2}^{\dagger} \sigma_y \otimes \sigma_y + {\alpha_3}^{\dagger} \sigma_z \otimes \sigma_z\right) && \text{(S23)} \\ &= \left(|\alpha_0|^2 + |\alpha_1|^2 + |\alpha_2|^2 + |\alpha_3|^2\right) I \otimes I + \left(\alpha_0 {\alpha_1}^{\dagger} + {\alpha_0}^{\dagger} \alpha_1 - \alpha_2 {\alpha_3}^{\dagger} - {\alpha_2}^{\dagger} \alpha_3\right) \sigma_x \otimes \sigma_x \\ &\quad + \left(\alpha_0 {\alpha_2}^{\dagger} + {\alpha_0}^{\dagger} \alpha_2 - \alpha_1 {\alpha_3}^{\dagger} - {\alpha_1}^{\dagger} \alpha_3\right) \sigma_y \otimes \sigma_y + \left(\alpha_0 {\alpha_3}^{\dagger} + {\alpha_0}^{\dagger} \alpha_3 - \alpha_1 {\alpha_2}^{\dagger} - {\alpha_1}^{\dagger} \alpha_2\right) \sigma_z \otimes \sigma_z && \text{(S24)} \end{aligned}$$

This gives that

$$|\alpha_0|^2 + |\alpha_1|^2 + |\alpha_2|^2 + |\alpha_3|^2 = 1 \tag{S25}$$

$$\alpha_0 {\alpha_1}^{\dagger} + {\alpha_0}^{\dagger} \alpha_1 - \alpha_2 {\alpha_3}^{\dagger} - {\alpha_2}^{\dagger} \alpha_3 = 0 \tag{S26}$$

$$\alpha_0 {\alpha_2}^{\dagger} + {\alpha_0}^{\dagger} \alpha_2 - \alpha_1 {\alpha_3}^{\dagger} - {\alpha_1}^{\dagger} \alpha_3 = 0 \tag{S27}$$

$$\alpha_0 {\alpha_3}^{\dagger} + {\alpha_0}^{\dagger} \alpha_3 - \alpha_1 {\alpha_2}^{\dagger} - {\alpha_1}^{\dagger} \alpha_2 = 0 \tag{S28}$$

which implies that the operation U_{LC} as defined in Equation (S21) is unitary. □

The circuit evolves as below (ignore P_1, P_2, Q_1 and Q_2 first), where $|\varphi_{12}\rangle$ is an arbitrary two-qubit state.

$$|00\rangle |\varphi_{12}\rangle \tag{S29}$$

$$\rightarrow \frac{1}{2} \left(|00\rangle + |01\rangle + |10\rangle + |11\rangle\right) |\varphi_{12}\rangle \tag{S30}$$

$$\rightarrow \frac{1}{2} \left(|00\rangle I \otimes I |\varphi_{12}\rangle + |01\rangle \sigma_x \otimes \sigma_x |\varphi_{12}\rangle + |10\rangle \sigma_y \otimes \sigma_y |\varphi_{12}\rangle + |11\rangle \sigma_z \otimes \sigma_z |\varphi_{12}\rangle\right) \tag{S31}$$

$$\begin{aligned} \rightarrow \frac{1}{2} &\left[\left(\alpha_0 |00\rangle + \alpha_1 |01\rangle + \alpha_2 |10\rangle + \alpha_3 |11\rangle\right) I \otimes I |\varphi_{12}\rangle + \left(\alpha_1 |00\rangle + \alpha_0 |01\rangle - \alpha_3 |10\rangle - \alpha_2 |11\rangle\right) \sigma_x \otimes \sigma_x |\varphi_{12}\rangle \right. \\ &\left. + \left(\alpha_2 |00\rangle - \alpha_3 |01\rangle + \alpha_0 |10\rangle - \alpha_1 |11\rangle\right) \sigma_y \otimes \sigma_y |\varphi_{12}\rangle + \left(\alpha_3 |00\rangle - \alpha_2 |01\rangle - \alpha_1 |10\rangle + \alpha_0 |11\rangle\right) \sigma_z \otimes \sigma_z |\varphi_{12}\rangle\right] \end{aligned} \tag{S32}$$

$$\begin{aligned} = \frac{1}{2} &\left[|00\rangle \left(\alpha_0 II + \alpha_1 \sigma_x \sigma_x + \alpha_2 \sigma_y \sigma_y + \alpha_3 \sigma_z \sigma_z\right) |\varphi_{12}\rangle + |01\rangle \left(\alpha_1 II + \alpha_0 \sigma_x \sigma_x - \alpha_3 \sigma_y \sigma_y - \alpha_2 \sigma_z \sigma_z\right) |\varphi_{12}\rangle + \right. \\ &\left. |10\rangle \left(\alpha_2 II - \alpha_3 \sigma_x \sigma_x + \alpha_0 \sigma_y \sigma_y - \alpha_1 \sigma_z \sigma_z\right) |\varphi_{12}\rangle + |11\rangle \left(\alpha_3 II - \alpha_2 \sigma_x \sigma_x - \alpha_1 \sigma_y \sigma_y + \alpha_0 \sigma_z \sigma_z\right) |\varphi_{12}\rangle\right] \end{aligned} \tag{S33}$$

Next, according to the measurement results (in the computational basis) of the two control qubits, different Pauli gates are applied to the two target qubits:

$$I \otimes I \left(\alpha_0 II + \alpha_1 \sigma_x \sigma_x + \alpha_2 \sigma_y \sigma_y + \alpha_3 \sigma_z \sigma_z\right) \rightarrow \alpha_0 II + \alpha_1 \sigma_x \sigma_x + \alpha_2 \sigma_y \sigma_y + \alpha_3 \sigma_z \sigma_z \tag{S34}$$

$$\left(\sigma_x \otimes \sigma_x\right) \left(\alpha_1 II + \alpha_0 \sigma_x \sigma_x - \alpha_3 \sigma_y \sigma_y - \alpha_2 \sigma_z \sigma_z\right) \rightarrow \alpha_0 II + \alpha_1 \sigma_x \sigma_x + \alpha_2 \sigma_y \sigma_y + \alpha_3 \sigma_z \sigma_z \tag{S35}$$

$$\left(\sigma_y \otimes \sigma_y\right) \left(\alpha_2 II - \alpha_3 \sigma_x \sigma_x + \alpha_0 \sigma_y \sigma_y - \alpha_1 \sigma_z \sigma_z\right) \rightarrow \alpha_0 II + \alpha_1 \sigma_x \sigma_x + \alpha_2 \sigma_y \sigma_y + \alpha_3 \sigma_z \sigma_z \tag{S36}$$

$$\left(\sigma_z \otimes \sigma_z\right) \left(\alpha_3 II - \alpha_2 \sigma_x \sigma_x - \alpha_1 \sigma_y \sigma_y + \alpha_0 \sigma_z \sigma_z\right) \rightarrow \alpha_0 II + \alpha_1 \sigma_x \sigma_x + \alpha_2 \sigma_y \sigma_y + \alpha_3 \sigma_z \sigma_z \tag{S37}$$

Therefore, the linear-combination operation $\alpha_0 II + \alpha_1\sigma_x\sigma_x + \alpha_2\sigma_y\sigma_y + \alpha_3\sigma_z\sigma_z$ can be implemented deterministically. Together with P_1, P_2, Q_1 and Q_2, the linear-combination operation $U = \sum_{i=0}^{3} \alpha_i \left(P_1\sigma_i Q_1\right) \otimes \left(P_2\sigma_i Q_2\right)$ can be implemented deterministically.

The two control qubits can be replaced by a single ququart and then U_{LC} can be implemented as a single-ququart operation. It is also worth-noting that there is no limits to the size of each linear term in principle and thus a deterministic linear-combination of four larger gates can be implemented similarly.

II. OPTICAL LINEAR-COMBINATION IMPLEMENTATION FOR UNIVERSAL TWO-QUBIT UNITARY GATES

A. Further discussion of optical linear-combination scheme

There are different degrees of freedom can be used to encode high-dimensional information in a single photon, such as polarization, time-bin and orbital angular momentum. On our silicon photonic chip, only spatial degree of freedom of photons is used, which can be easily to expand to high dimensions[4] and thus is particularly suitable for the Hilbert space extension used in the linear-combination scheme. It would be an interesting open question whether other degrees of freedom of a single photon could be combined with the spatial mode freedom on silicon photonic device to explore more computation capability.

The optical linear-combination scheme is more resource-efficient than other existing optical schemes for implementing universal two-qubit unitaries. We compare it with two main schemes for universal linear optical quantum computing: the KLM scheme and MBQC scheme. In standard quantum circuit model, the universal two-qubit quantum circuit requires at least three CNOT and eight single-qubit gates[5], as shown in Fig. S1(A). In linear optical systems, a CNOT or other equivalent two-qubit-entangling logic gates[6] can only be implemented probabilistically, if requiring no optical nonlinearity[7]. KLM scheme implements a CNOT gate probabilistically on coincidence detection of ancillary photons at two single photon detectors, and the success probability is 1/16[7]. There are also some other protocols proposed for implementing CNOT gate with no optical nonlinearity, such as the protocols proposed by T. B. Pittman *et al.*[8] and by Hofmann & Takeuchi[9] and by T. C. Ralph *et al.*[10]. Pittman's protocol utilizes four photons and implements a CNOT with the success probability of 1/4. Ralph's and Hofmann & Takeuchi's protocol implements a CNOT by using only two photons with the success probability of 1/9. However, post-selection of the coincidence events was required, and thus it cannot be used for implementing cascaded CNOT gates. Therefore, the most resource-efficient way for implementing a quantum circuit shown in Fig. S1(A) is to use two Pittman CNOT gates and one post-selected CNOT gate, which requires 6 photons totally and has the overall success probability of 1/144.

MBQC scheme differs from standard quantum circuit model[11–15], which implements quantum computation by performing a sequence of single-qubit measurements onto the prepared cluster state. MBQC is less demanding of resources than the standard circuit model[16]. However, MBQC requires at least a 6-photon cluster state (Fig. S1(B)) to implement the computation equivalent to the universal two-qubit circuit shown in Fig. S1(A). It needs more photons to create such a state, and has low success probability as 1/128, where we assume the required cluster state is created via Type-I fusion[16] with success probability of 1/2 each.

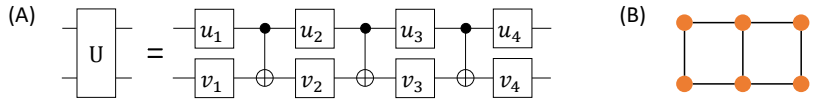

FIG. S1: (A) Quantum circuit for universal two-qubit quantum operation $U \in \mathrm{SU}(4)$, requiring three consecutive CNOT gates and eight single-qubit gates u_i and v_i $(i = 1, \cdots, 4)$[5]. (B) A six-photon cluster state required for implementing QIP that utilizes at least three two-qubit entangling operations in MBQC scheme.

B. Advanced photonic linear-combination circuit design for higher success probability

Our current chip implements a two-qubit unitary operation with success probability of 1/64. It can be further improved to 1/4, if we (i) can separate signal and idler photons with certainty; (ii) use an advanced circuit design as shown in Fig. S2. The new circuit design will utilize the unused optical ports (in our current chip), and the circuit succeeds when the coincidence detections happen between the ports 1 and 2 or $1'$ and $2'$ or $1''$ and $2''$ or $1'''$ and $2'''$.

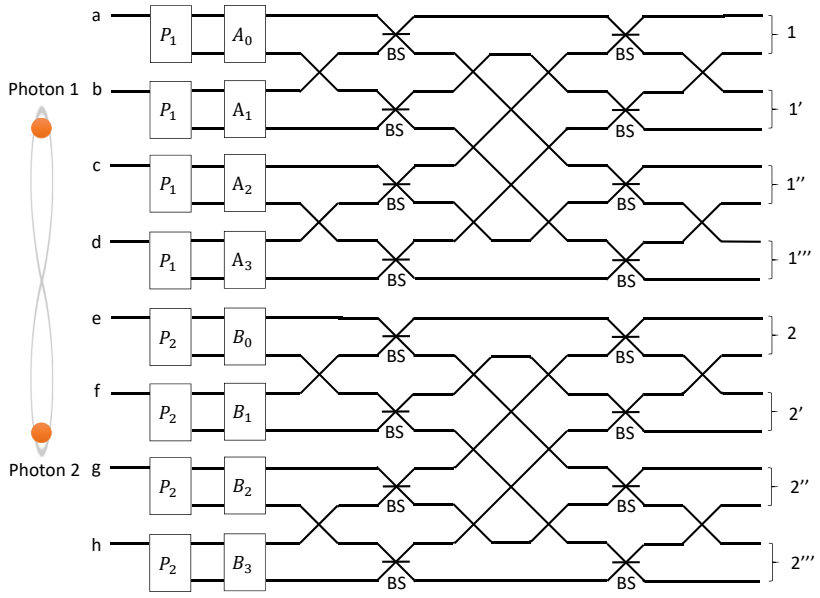

FIG. S2: Schematic of an advanced circuit design for implementing SU(4). The entangled ququarts creation part and tomography measurement part are omitted. Assume photon in top path represents the basis state $|0\rangle$ and the bottom represents $|1\rangle$, P_1 and P_2 convert the single-qubit state $|0\rangle$ into two arbitrary single-qubit states $|\varphi_1\rangle$ and $|\varphi_2\rangle$ respectively. A_0 - A_3, B_0 - B_3 are single-qubit operations. The linear-combination operation succeeds when the coincidence events detected where two photons exit at ports 1, 2 (or 1′, 2′; 1″, 2″; 1‴, 2‴) respectively.

III. LINEAR-COMBINATION SCHEME FOR LARGE-SCALE QUANTUM COMPUTATION

The linear-combination scheme introduces a promising implementation of large-scale quantum information processing applications, though in the implemented form it does not target the ultimate universal quantum computer due to the fact that it would achieve exponentially small success probability for a universal quantum computer. Nevertheless it can implement families of large-scale quantum information processing applications with considerable success probability. Here we show how to generalise the linear-combination scheme for large-scale quantum computation and illustrate an example of a 4-qubit version of the linear-combination scheme.

One way for scaling up the linear-combination scheme is to enlarge the size of the individual linear-combination terms. Such an approach could be fruitful with advances in photon production technology. However, considering that we are currently seeking an optical scheme with limited photon sources, a better choice would be to exploit the high-dimensional degrees of freedom of a single photon to encode qudits, for which a 15-dimensional qudit encoded in the spatial modes of a single photon has been demonstrated[4]. On the silicon quantum photonic platform, spatial modes are ideal for encoding high-dimension qudit state. These high-dimension qudit states can be generated, manipulated and measured through a Reck-scheme universal linear optic implementation[17,18]. With these enlarged linear-combination terms, we are able to realise larger quantum computation applications even though the single photons are quite limited. For example, a two-term linear combination $\frac{1}{\sqrt{2}}(I_4 \otimes I_4 + Z_4 \otimes Z_4)$, with I_4 being a 4-dimensional identity gate and $Z_4 = Z \otimes Z$ where Z is pauli-Z gate, can equivalently implement a four-qubit operation which filters out the states in all 16 computational basis states that have an odd number of qubits being in $|1\rangle$. On the other hand, we can also increase the number of the linear terms to increase the computation capability of a linear-combination implementation, though it has only limited utility since it meanwhile decreases the success probability in a reciprocal relationship with the number of terms.

Families of unitary operations can be decomposed into a small number of linear-combination terms, for example, an arbitrary controlled-unitary gate CU can be expressed as a linear combination of two terms:

$$\mathrm{CU} = \tfrac{1}{\sqrt{2}}\begin{pmatrix}1 & 0\\ 0 & i\end{pmatrix} \otimes \tfrac{I-iU}{\sqrt{2}} + \tfrac{1}{\sqrt{2}}\begin{pmatrix}1 & 0\\ 0 & -i\end{pmatrix} \otimes \tfrac{I+iU}{\sqrt{2}},$$

where U is the target operation and arbitrary-sized and U can be implemented by a Reck-scheme universal linear interaction. Another specific example is the four-qubit gate $\mathrm{C^3Z}$ which introduces a sign flip if and only if all four

qubits are in the computational basis state $|1\rangle$. Its gate matrix is shown as below:

$$\mathrm{C^3Z} = \begin{pmatrix} 1&0&0&0&0&0&0&0&0&0&0&0&0&0&0&0 \\ 0&1&0&0&0&0&0&0&0&0&0&0&0&0&0&0 \\ 0&0&1&0&0&0&0&0&0&0&0&0&0&0&0&0 \\ 0&0&0&1&0&0&0&0&0&0&0&0&0&0&0&0 \\ 0&0&0&0&1&0&0&0&0&0&0&0&0&0&0&0 \\ 0&0&0&0&0&1&0&0&0&0&0&0&0&0&0&0 \\ 0&0&0&0&0&0&1&0&0&0&0&0&0&0&0&0 \\ 0&0&0&0&0&0&0&1&0&0&0&0&0&0&0&0 \\ 0&0&0&0&0&0&0&0&1&0&0&0&0&0&0&0 \\ 0&0&0&0&0&0&0&0&0&1&0&0&0&0&0&0 \\ 0&0&0&0&0&0&0&0&0&0&1&0&0&0&0&0 \\ 0&0&0&0&0&0&0&0&0&0&0&1&0&0&0&0 \\ 0&0&0&0&0&0&0&0&0&0&0&0&1&0&0&0 \\ 0&0&0&0&0&0&0&0&0&0&0&0&0&1&0&0 \\ 0&0&0&0&0&0&0&0&0&0&0&0&0&0&1&0 \\ 0&0&0&0&0&0&0&0&0&0&0&0&0&0&0&-1 \end{pmatrix}$$

$\mathrm{C^3Z}$ gate can be decomposed into a six-term linear combination of $\mathrm{SU(4)} \otimes \mathrm{SU(4)}$ operations: $\mathrm{C^3Z} = \sum_{i=0}^{5} \alpha_i A_i \otimes B_i$, where α_i, A_i and B_i are listed in Table I. Such a six-term linear combination can be implemented by using a two-photon six-dimensional entanglement that can be created via the same way used here in building the universal 2-qubit photonic quantum processor. In Fig. S3 we present a specific optical implementation scheme for realising such six-term linear combination where the creation of two-photon six-dimensional entanglement has been omitted. As shown in the theoretical diagram, a 4-dimensional Reck-scheme universal linear optics implementation is used as the basic unit to prepare single-ququart states and perform single-ququart operations and also perform single-ququart measurements. It uses only 154 phase shifters theoretically to implement $\mathrm{C^3Z}$ gate using such linear-combination scheme —10 phase shifters for two-photon six-dimensional entanglement generation and 144 phase shifters for 12 SU(4) operation realisations. A family of four-qubit quantum circuits can be constructed using the $\mathrm{C^3Z}$ gate, including the four-qubit Tofolli gate[19]. They all can be decomposed into a six-term linear combination and can be implemented using the proposed optical scheme shown in Fig. S3, with theoretical success probability as high as 1/6.

TABLE I: Linear-combination decomposition result of the $\mathrm{C^3Z}$ gate.

Linear-combination coefficient α_i	A_i	B_i
0.5	$A_0 = \begin{pmatrix} 1&0&0&0 \\ 0&1&0&0 \\ 0&0&i&0 \\ 0&0&0&i \end{pmatrix}$	$B_0 = \begin{pmatrix} 1&0&0&0 \\ 0&1&0&0 \\ 0&0&1&0 \\ 0&0&0&1 \end{pmatrix}$
0.5	$A_1 = \begin{pmatrix} 1&0&0&0 \\ 0&1&0&0 \\ 0&0&-i&0 \\ 0&0&0&-i \end{pmatrix}$	$B_1 = \begin{pmatrix} 1&0&0&0 \\ 0&1&0&0 \\ 0&0&1&0 \\ 0&0&0&1 \end{pmatrix}$
$-\frac{i}{2\sqrt{2}}$	$A_2 = \begin{pmatrix} 1&0&0&0 \\ 0&i&0&0 \\ 0&0&i&0 \\ 0&0&0&-1 \end{pmatrix}$	$B_2 = \frac{1}{\sqrt{2}} \begin{pmatrix} 1-i&0&0&0 \\ 0&1-i&0&0 \\ 0&0&1-i&0 \\ 0&0&0&1+i \end{pmatrix}$
$-\frac{i}{2\sqrt{2}}$	$A_3 = \begin{pmatrix} 1&0&0&0 \\ 0&-i&0&0 \\ 0&0&i&0 \\ 0&0&0&1 \end{pmatrix}$	$B_3 = \frac{1}{\sqrt{2}} \begin{pmatrix} 1+i&0&0&0 \\ 0&1+i&0&0 \\ 0&0&1+i&0 \\ 0&0&0&1-i \end{pmatrix}$
$\frac{i}{2\sqrt{2}}$	$A_4 = \begin{pmatrix} 1&0&0&0 \\ 0&i&0&0 \\ 0&0&-i&0 \\ 0&0&0&1 \end{pmatrix}$	$B_4 = \frac{1}{\sqrt{2}} \begin{pmatrix} 1-i&0&0&0 \\ 0&1-i&0&0 \\ 0&0&1-i&0 \\ 0&0&0&1+i \end{pmatrix}$
$\frac{i}{2\sqrt{2}}$	$A_5 = \begin{pmatrix} 1&0&0&0 \\ 0&-i&0&0 \\ 0&0&-i&0 \\ 0&0&0&-1 \end{pmatrix}$	$B_5 = \frac{1}{\sqrt{2}} \begin{pmatrix} 1+i&0&0&0 \\ 0&1+i&0&0 \\ 0&0&1+i&0 \\ 0&0&0&1-i \end{pmatrix}$

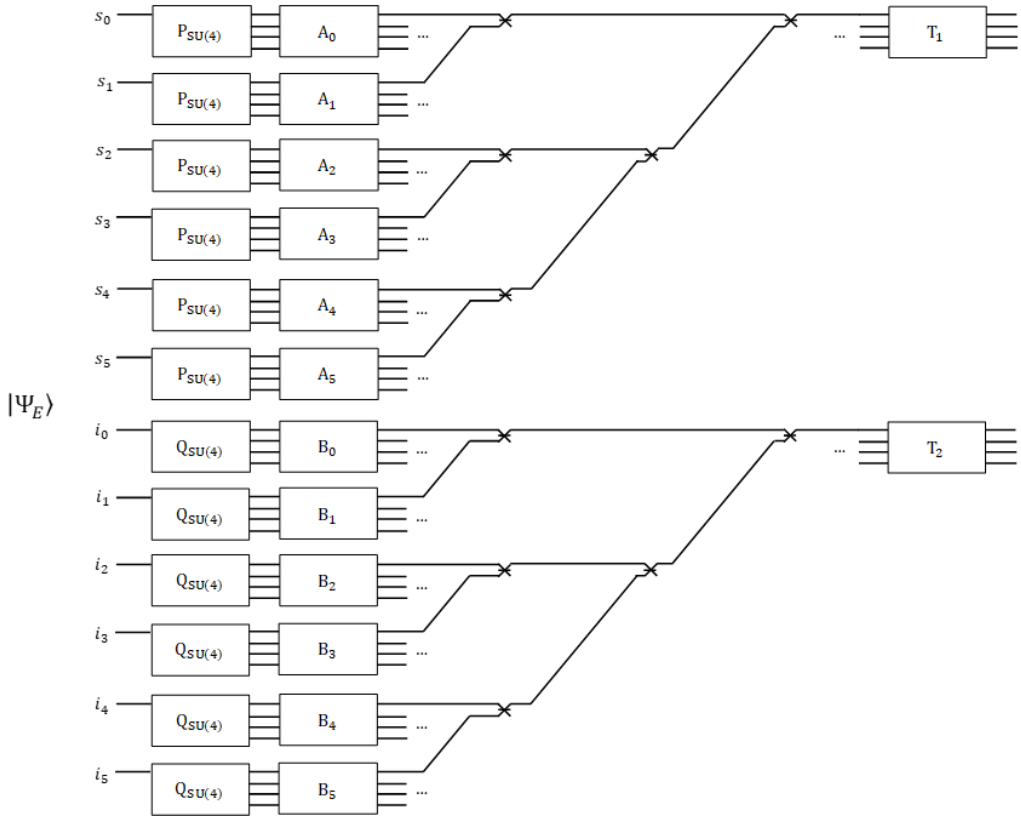

FIG. S3: A schematic diagram of implementing a 4-qubit gate using the linear-combination approach, with the reconfigurable bipartite six-dimension-entanglement generation part omitted. Here $|\Psi_E\rangle$ represents a bipartite six-dimensional entangled state $\sum_{t=0}^{5} \alpha_t |s_t\rangle \otimes |i_t\rangle$, where $|s_t\rangle$ and $|i_t\rangle$ represent spatial modes of signal and idler photons. $P_{\mathrm{SU}(4)}$, $Q_{\mathrm{SU}(4)}$, A_i, B_i and T_1, T_2 are four-dimensional Reck-scheme circuits that can implement universal four-dimensional universal linear optical operations. $P_{\mathrm{SU}(4)}$, $Q_{\mathrm{SU}(4)}$ are used to prepare arbitrary separable two-ququart states. T_1, T_2 are used to perform arbitrary ququart tomography measurement. A_i, B_i, together with the state $|\Psi_E\rangle$ and post-selection, are used to implement a 4-qubit operation U in the form of $\sum_{i=0}^{5} \alpha_i A_i \otimes B_i$.

IV. DETAILS OF DEVICE AND EXPERIMENTAL SETUP

A. Device

Our silicon chip was fabricated using a 248 nm lithography at the IME foundry. The starting substrate is silicon-on-insulator (SOI) substrate with 2 μm buried oxide (BOX) and 220 nm top crystalline Si on BOX. The 500-nm-wide silicon waveguides were patterned in the 220-nm top layer of silicon. Resistive heaters working as thermo-optic phase shifters, 180 μm long and 2.5 μm wide, are then patterned on a 120 nm TiN metal layer on top of the waveguide layer. The effective footprint of the device is approximately 7.1×1.9 mm^2.

The propagation loss for channel waveguide is 3 dB/cm in our device. The multi-mode interferometers (MMI) in the device has around 0.3 dB insertion loss. The thermo-optic phase shifters have ignorable loss compared to the MMIs. The electric power required for 2π phase shift for one individual thermo-optic phase shifter is around 57 mW. All the thermo-optic phase shifters each have about 800 Ω resistance and the applied current for 2π phase shift is less than 10 mA.

B. Setup

The schematic diagram of the whole setup was shown in Fig. 1(D) in the main text. Bright light with the wavelength of 1550.8 nm is collected from a tunable laser (Yenista Optics Tunics-T100S-HP) and further amplified using an EDFA (Pritel), up to 300 mW. The amplified spontaneous emission (ASE) noise is suppressed using a DWDM module filter (Opneti). The bright light is then injected into the silicon chip via a 48-channel V-Groove fiber array (OZ-optics)

with 127 μm spacing and 10-degree angle polished from top to bottom. An in-line polarization controller (FiberPro) is used to ensure that TE-polarized light is launched into the chip through TE grating couplers fabricated on the chip.

At the end of the optical output of the chip, two off-chip DWDM module filters, having a 200 GHz channel space and 1 nm 0.5 dB bandwidth, are used to separate the signal and idler photons. We chose the channels that are equally 4-channels away from the channel used for the pump light for selecting the signal and idler photons respectively: $\lambda_p - \lambda_s = \lambda_i - \lambda_p = 6.6$ nm. We only picked up the signal photons ($\lambda_s = 1544.2$ nm) through one DWDM filter (DWDM_1) and the idler photons ($\lambda_i = 1557.4$ nm) through the other (DWDM_2), realizing the post-selected measurements. Note that we can also pick up the idler photons from (DWDM_1) and the signal photons from (DWDM_2) to realize post-selection, which can in theory double the coincidence counts but require two extra single-photon detectors.

For the signal photon channel and the idler photon channel, the insertion losses over full passband are 1.89 dB and 2.88 dB respectively. Both of the DWDM filters have ≥ 45 dB isolation over full passband for non-adjacent channels. Together with the on-chip pump filters, the pump injected to the chip are effectively isolated from the photon detections. The coupling loss of our device (including both input and output) is 13 dB, which is estimated by injecting pump light through V-Groove fiber array to a long straight waveguide surrounding our device on the silicon chip. Chip expansion happens when the phase shifters are heated up, and thus introduces instability of optical coupling. To overcome this issue, we used a Peltier cell controlled by a proportional integrative derivative (PID) controller to keep the device temperature constant actively.

The photons are detected by two fiber-coupled superconducting nanowire single-photon detectors (SNSPDs) mounted in a closed cycle refrigerator. Two in-line polarization controllers are used to optimize the polarizations of photons before going into SNSPDs, which maximizes the detection efficiency up to 50%. Two-photon coincidences are recorded by using a time-interval-analyzer (PicoHarp 300) in a 450 ps integration window, which was chosen according to the jitter-time of SNSPDs. During the experiments, the dark count for single photon detection is 800-1500 per second, but is quite trivial for the two-photon coincidence events. Upon using 300 mW pump power, we obtain around 100 coincidence counts per second during the experiments.

V. CHARACTERIZATION OF THE DEVICE

A. Electrical characteristics of the phase shifters

Characterization is critical for integrated quantum photonic devices. In our device, the main task is to calibrate the electric power-optics responses of the phase shifters, i.e., find the corresponding phase of a phase shifter for each applied voltage or current. All the thermal-optic phase shifters are controlled by 62-channel current output equipment (UEI AO current boards), which allows to set the required current to each channel via serial communication from a classical computer.

We first measured the resistance value of each phase shifter by scanning its I-V curve. The I-V curve of an example phase shifter is shown in Fig. S4, showing perfect linearity. The obtained I-V curve can be simply fitted into a linear

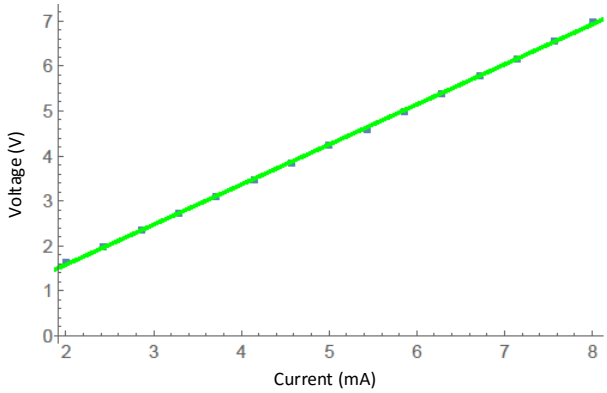

FIG. S4: The measured I-V curve of an example thermal-optic phase shifter. The horizontal axis represents the current applied to the phase shifter and the vertical axis represents the measured voltage.

equation as

$$V = R \cdot I + \delta V \tag{S38}$$

where R represents the resistance value of the phase shifter and δV represents the offset of the voltage of the current output boards with 0 mA current setting. The fitted resistances of all the phase shifters in our device are around 800 Ω, except that the four phase shifters used in the pump filters have resistance values of around 580 Ω.

Thermal-optic phase shifter has a linear phase-(electrical)power relationship and further a nonlinear phase-current relationship, considering the fact that elect-power of a phase shifter is given by

$$P = I^2 R. \tag{S39}$$

Therefore, the phase-current relationship of a phase shifter can be obtained as

$$\theta(I) = \phi_1 I^2 + \phi_0 \tag{S40}$$

where I is the current applied to the phase shifter and $\theta(I)$ is the resulting phase shift. ϕ_1 and ϕ_0 are real numbers associated with the response of a particular phase shifter.

All the 62 thermal-optic phase shifters are divided into two kinds: independent phase shifters and cascaded phase shifters. Here we say an independent phase shifter is the one occupying a MZI whose input and output can be directly accessed by external laser and optical power-meter. For the independent phase shifter, we assume the associated MMIs have good splitting ratio close to 50:50. In fact, we measured that such an independent MZI in our device can achieve an extinction ratio up to 30 dB[20].

B. Calibrating independent phase shifters

An example independent phase shifter is shown in Fig. S5(A), where we can directly inject bright light (1550 nm, 20 mW) into one input port (for example, In1) of the MZI and measure the intensity at one output port (Out1) as a function of the current applied to the heater. The applied current increases linearly from 0 mA to 9 mA with the step size of 0.05 mA. The obtained classical interference fringe of one example independent phase shifter is shown in Fig. S5(B).

Using nonlinear fitting approach (such as Mathematica built-in function: NonlinearModelFit), we were able to fit the experimental data with Equation (S40), obtaining that $\phi_1 = 0.1123$ and $\phi_0 = 0.3814$. In our device, the phase shifters used in the four filters, in setting the laser intensities between four SFWM sources and in the stage of performing measurement are independent phase shifters that can be calibrated directly. The phase shifters in setting phases between four SFWM sources and in the stage of realizing linear-combination can also be calibrated as the independent phase shifter once the cascaded phase shifters in the stages of preparing single-qubit states and implementing operations were calibrated, which we will discuss in the following section.

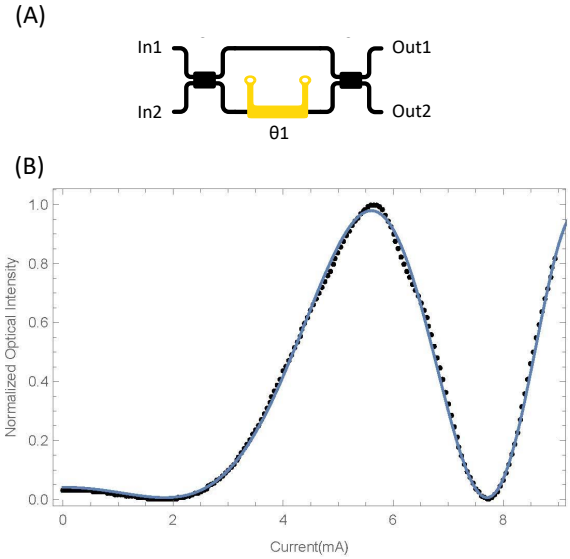

FIG. S5: (A) Schematic diagram of an independent phase shifter occupying in an MZI. (B) The current optical-intensity fringe curve of an example independent phase shifter. The black points represent the experimental data and the blue curve is obtained through the fitting function, showing a good fitness.

C. Calibrating cascaded phase shifters

The cascaded phase shifters illustrated in Fig. S6 the five phase shifters located in an array—used in the stages of preparing single-qubit state and implementing gates, as shown in the Fig. 1(D) in the main text. Here we present a schematic diagram of such cascaded phase shifters in Fig. S6. There are eight cascaded phase shifter arrays in our device. These phase shifters cannot be simply calibrated like the independent ones, since we can only access the input and output ports of the whole array.

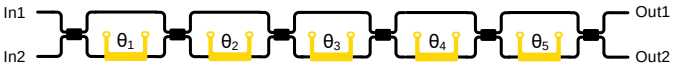

FIG. S6: Schematic of five cascaded phase shifters in an array.

To calibrate these phase shifters, we scanned a 5-dimensional (5D) fringe for each array and performed multiple parameters fitting. In the 5D scan, we scan same current range for each of the five phase shifters and record the experimentally obtained output power for every current configuration. This 5D scan fitting approach works well for our device, but it may be challenging for a larger number of cascaded phase shifters since it requires exponentially-increasing amount of data.

Specifically, we injected the classical light into one input port (In1) and measured the output intensity at one output port (Out1). For a current configuration of the five phase shifters $\{I_1, I_2, I_3, I_4, I_5\}$, we measured the corresponding output intensity. A least-square minimization algorithm was used to fit the measured optical intensities and theoretical values, and thus the fitted parameters associated with the responses of the phase shifters can be estimated. The theoretical transfer matrix of the cascaded phase shifters is given by

$$\begin{aligned} &U_{\text{Array}}[\eta_0, \eta_1, \eta_2, \eta_3, \eta_4, \eta_5, \theta_1, \theta_2, \theta_3, \theta_4, \theta_5] \\ &= \text{BS}[\eta_5]\text{PS}[\theta_5]\text{BS}[\eta_4]\text{PS}[\theta_4]\text{BS}[\eta_3]\text{PS}[\theta_3]\text{BS}[\eta_2]\text{PS}[\theta_2]\text{BS}[\eta_1]\text{PS}[\theta_1]\text{BS}[\eta_0] \end{aligned} \tag{S41}$$

where BS and PS define the transfer matrices of MMI beam-splitter and phase shifter as follows:

$$\text{BS}[\eta] := \begin{pmatrix} \sqrt{\eta} & i\sqrt{1-\eta} \\ i\sqrt{1-\eta} & \sqrt{\eta} \end{pmatrix}, \tag{S42}$$

$$\text{PS}[\theta] := \begin{pmatrix} 1 & 0 \\ 0 & e^{i\theta} \end{pmatrix}. \tag{S43}$$

Note that here η represents the splitting ratio of each MMI, which is close to 50:50 and independent of applied current. θ_i represents the phase setting of the corresponding phase shifter, which is given by

$$\theta_i = \phi_i(I_i^2 R_i) + \delta\theta_i \tag{S44}$$

where I_i is the current applied to the heater i with resistance value R_i, and $\delta\theta_i$ is the phase offset when zero-current applied.

The objective function of minimization is thus obtained as

$$\text{Min}\left(\sum_m \left(O_m - A \cdot |\langle 0| U_{\text{Array}}[\eta_0, \eta_1, \eta_2, \eta_3, \eta_4, \eta_5, \theta_1, \theta_2, \theta_3, \theta_4, \theta_5] |0\rangle|^2\right)^2\right) \tag{S45}$$

where O_m is normalized experimentally obtained optical intensity and θ_i is replaced by using Equation (S44). The minimization process can be implemented using the Mathematica built-in function "FindMinimun" with proper initial guess. After the fitting process, we obtain the fitted results for the parameters η_0, η_1, η_2, η_3, η_4, η_5, ϕ_1, $\delta\theta_1$ ϕ_2, $\delta\theta_2$ ϕ_3, $\delta\theta_3$ ϕ_4, $\delta\theta_4$ ϕ_5, $\delta\theta_5$. These 16 parameters are able to describe the behaviors of the response of the calibrated cascaded phase shifter array for each current configuration, making each phase shifter in the array fully reconfigurable.

D. Calibrating on-chip filters

In our device, the on-chip filters are used to remove the redundant pump light out from the photon sources.The on-chip pump filter is implemented by using an imbalanced MZI, as shown in Fig S7.

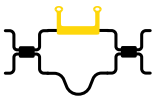

FIG. S7: Schematic of the on-chip pump filter. On the actual silicon chip, the arm where the phase shifter locates is 54 μm longer than the other arm of MZI.

With a proper current applied, the imbalanced MZI has different transmission responses for different wavelengths of light, as shown in Fig. S8. It shows that the pump filter has very low transmission rate for the light with wavelength around 1550.8 nm but high transmission rate for the light with wavelengths around 1544.2 nm and 1557.4 nm—which corresponds to the signal and idler photons respectively. The extinction ratio of the pump filter is up to $\sim$ 28 dB, which filters the pump light after the photon sources quite effectively. In the experiments, we used a laser pump of up to 300 mW (24.77 dBm) for each SFWM photon source. After the on-chip pump filter, there is $\sim$ 0.475 mW (-3.223 dBm) pump light passing through the functional area of the device (states and operations configuration and measurement, marked 2 to 5 in Figure 1 D of the main text). This is a very small intensity of pump which only generates trivial SFWM effect during the waveguides in the functional area, adding negligible counts to the signal that are suppressed through our measurement of the coincidence counts between signal and idler photons generated from the same source—the signal photon and the idler photon of the same pair pass through the top half and bottom half of the device separately. But the photon pairs generated from remnant of the pump will always pass through the same half of the device, top or bottom, which is impossible to cause a coincidence count in our detection setup.

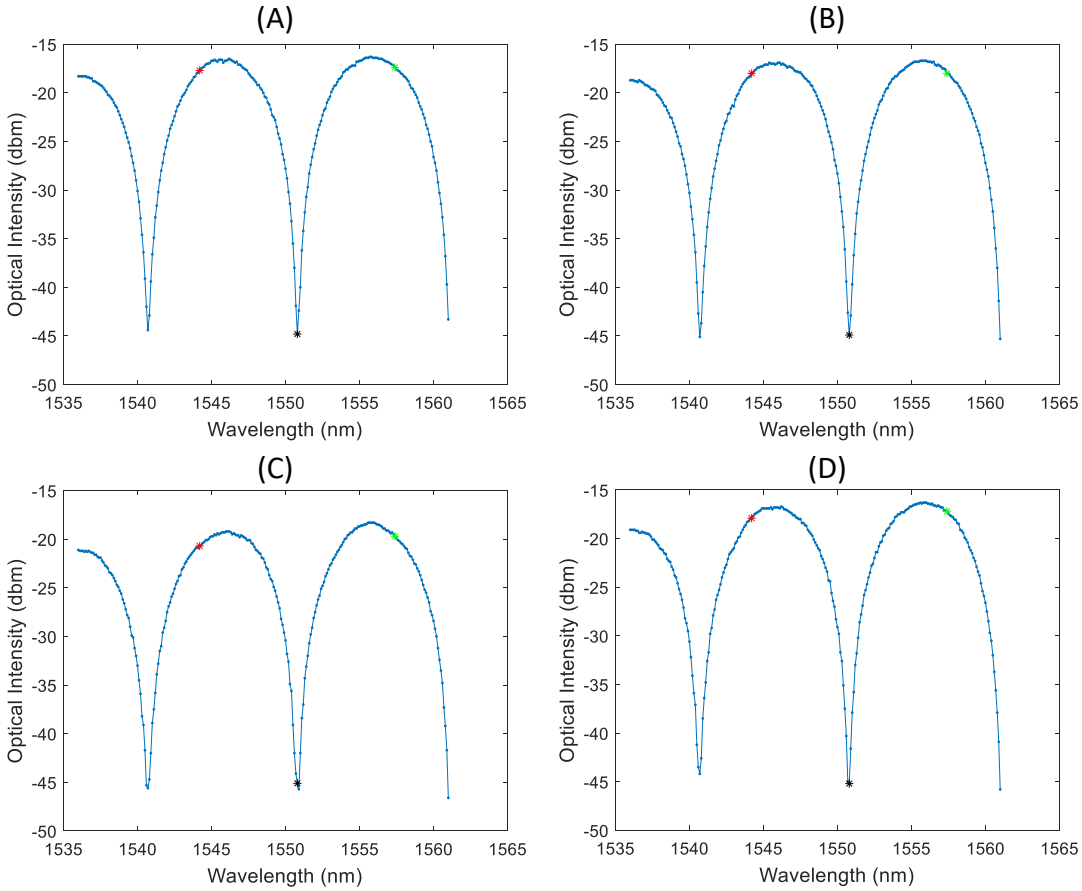

FIG. S8: Transmission responses of the four on-chip pump filters with wavelengths. The pump light is injected into the top input port and is measured at the top output port. The red, green and black stars in figures mark the signal, idler and pump wavelengths respectively.

VI. FURTHER DETAILS OF EXPERIMENTAL QUANTUM PROCESSING RESULTS

A. Implementing two-qubit quantum logic gates

Here we first present details for implementing some specific quantum gates: CNOT, CZ, CH, SWAP, iSWAP and $\sqrt{\text{SWAP}}$. The linear-combination decompositions of CNOT, CZ and CH are listed as follows:

$$\text{CNOT} = \frac{1}{\sqrt{2}}\begin{pmatrix}1 & 0\\ 0 & i\end{pmatrix} \otimes \frac{1}{\sqrt{2}}\begin{pmatrix}1 & -i\\ -i & 1\end{pmatrix} + \frac{1}{\sqrt{2}}\begin{pmatrix}1 & 0\\ 0 & -i\end{pmatrix} \otimes \frac{1}{\sqrt{2}}\begin{pmatrix}1 & i\\ i & 1\end{pmatrix} \tag{S46}$$

$$\text{CZ} = \frac{1}{\sqrt{2}}\begin{pmatrix}1 & 0\\ 0 & i\end{pmatrix} \otimes \frac{1-i}{\sqrt{2}}\begin{pmatrix}1 & 0\\ 0 & i\end{pmatrix} + \frac{1}{\sqrt{2}}\begin{pmatrix}1 & 0\\ 0 & -i\end{pmatrix} \otimes \frac{1+i}{\sqrt{2}}\begin{pmatrix}1 & 0\\ 0 & -i\end{pmatrix} \tag{S47}$$

$$\text{CH} = \frac{1}{\sqrt{2}}\begin{pmatrix}1 & 0\\ 0 & i\end{pmatrix} \otimes \frac{1}{\sqrt{2}}\begin{pmatrix}\sqrt{2}-i & -i\\ -i & \sqrt{2}+i\end{pmatrix} + \frac{1}{\sqrt{2}}\begin{pmatrix}1 & 0\\ 0 & -i\end{pmatrix} \otimes \frac{1}{\sqrt{2}}\begin{pmatrix}\sqrt{2}+i & i\\ i & \sqrt{2}-i\end{pmatrix} \tag{S48}$$

To implement these gates in our device, we first configured the device to to create the following maximally path-entangled state:

$$\frac{1}{\sqrt{2}}|1\rangle_a|1\rangle_e + \frac{1}{\sqrt{2}}|1\rangle_b|1\rangle_f, \tag{S49}$$

and then programmed the local single-qubit operations on path a, b, e and f, following Equations (S46), (S47) and (S48). The initial input states for computation can be arbitrarily configured through the state preparation stages (including the first two phase shifters in each cascaded phase shifter array). The obtained process fidelities for these three gates are 98.85±0.06%, 96.90±0.17% and 97.57±0.07% respectively.

It is the first time for implementing SWAP, iSWAP and $\sqrt{\text{SWAP}}$ gates in integrated photonics chips. In standard quantum circuit model, a SWAP gate is implemented by a sequence of three CNOT gates where the middle one reverses the control and target qubits. An iSWAP gate can be implemented by a unitary gate $(I \otimes I - i\sigma_z \otimes \sigma_z)$ followed by a SWAP gate. $\sqrt{\text{SWAP}}$ gate performs half-way of SWAP, which allows for universal quantum computation together with single-qubit gates. The corresponding transfer matrices of these three gates are as follows.

$$\text{SWAP} = \begin{pmatrix}1 & 0 & 0 & 0\\ 0 & 0 & 1 & 0\\ 0 & 1 & 0 & 0\\ 0 & 0 & 0 & 1\end{pmatrix},\ \text{iSWAP} = \begin{pmatrix}1 & 0 & 0 & 0\\ 0 & 0 & i & 0\\ 0 & i & 0 & 0\\ 0 & 0 & 0 & 1\end{pmatrix},\ \sqrt{\text{SWAP}} = \begin{pmatrix}1 & 0 & 0 & 0\\ 0 & \frac{1+i}{2} & \frac{1-i}{2} & 0\\ 0 & \frac{1-i}{2} & \frac{1+i}{2} & 0\\ 0 & 0 & 0 & 1\end{pmatrix} \tag{S50}$$

The linear-combining decompositions of the three gates are

$$\text{SWAP} = \frac{1}{2}(I \otimes I + \sigma_x \otimes \sigma_x + \sigma_y \otimes \sigma_y + \sigma_z \otimes \sigma_z) \tag{S51}$$

$$\text{iSWAP} = \frac{1}{2}(I \otimes I + i\sigma_x \otimes \sigma_x + i\sigma_y \otimes \sigma_y + \sigma_z \otimes \sigma_z) \tag{S52}$$

$$\sqrt{\text{SWAP}} = (0.75+0.25i)I \otimes I + (0.25-0.25i)\sigma_x \otimes \sigma_x + (0.25-0.25i)\sigma_y \otimes \sigma_y + (0.25-0.25i)\sigma_z \otimes \sigma_z \tag{S53}$$

all of which are simple linear-combinations of tensor products of Pauli gates and identity gates.

For implementing SWAP and iSWAP, balanced pumps were split between the four photon sources with zero relative phase (SWAP) or $\pi/2$ relative phase (iSWAP), creating the following maximally path-entangled states:

$$\text{SWAP}: \ \frac{1}{2}|1\rangle_a|1\rangle_e + \frac{1}{2}|1\rangle_b|1\rangle_f + \frac{1}{2}|1\rangle_c|1\rangle_g + \frac{1}{2}|1\rangle_d|1\rangle_h \tag{S54}$$

$$\text{iSWAP}: \ \frac{1}{2}|1\rangle_a|1\rangle_e + \frac{i}{2}|1\rangle_b|1\rangle_f + \frac{i}{2}|1\rangle_c|1\rangle_g + \frac{1}{2}|1\rangle_d|1\rangle_h \tag{S55}$$

For implementing $\sqrt{\text{SWAP}}$, the path-entangled state will be required as

$$(0.75+0.25i)|1\rangle_a|1\rangle_e + (0.25-0.25i)|1\rangle_b|1\rangle_f + (0.25-0.25i)|1\rangle_c|1\rangle_g + (0.25-0.25i)|1\rangle_d|1\rangle_h \tag{S56}$$

and thus requires unbalanced pumps split between the four photon sources. The obtained process fidelities of SWAP, iSWAP and $\sqrt{\text{SWAP}}$ are 95.33±0.24%, 94.45±0.27%, 92.41±0.33% respectively. The reconstructed process matrices of these implemented gates are shown in Fig. S9.

For showcasing performance of the chip, we also implemented many other two-qubit quantum logic gates. These gates include four different kinds of gates, which are in the forms of $A_1 \otimes B_1$, Controlled-U, $\alpha A_1 \otimes A_2 + \beta B_1 \otimes B_2$ and $\alpha A_1 \otimes A_2 + \beta B_1 \otimes B_2 + \gamma C_1 \otimes C_2 + \delta D_1 \otimes D_2$ respectively. Here A_1 (A_2), B_1 (B_2), C_1 (C_2), D_1 (D_2), U, α, β, γ and δ are randomly chosen for each instance of the tested gates. These gates utilize a quarter, a half or full capability of the chip, demonstrating the full performance of the chip in various cases. Together with the specific gates mentioned above, we implemented 98 two-qubit quantum logic gates, performed quantum process tomography and reconstructed the corresponding process matrices for each instance, achieving the process fidelity of 93.15±4.53% in average. During the experiments, the typical integration time for each count of process tomography is 10 seconds, and the total cost time for performing full quantum process tomography for one tested gate is more than 100 minutes.

One straightforward factor that limits the experimental fidelities is the device fabrication, particularly the precision of MMIs. The imperfection of MMI can reduce the extinction ratio of a MZI whose typical value was obtained to be around 30 dB on our device. It can be overcome by using a MZI as a variable MMI—we had achieved up to 60 dB extinction ratio of a MZI with such "variable MMIs" on a device with same fabrication process[20]. Another main factor affecting the experimental fidelity is the precision of control of the phase shifters from two specific aspects: the calibration of and the thermal crosstalk between phase shifters. A 5-dimensional fringe and 16-parameter fitting approach was used to calibrate the arrays of five cascaded phase shifters. Accuracy of such calibration is limited by the amount of data where we used only 10^5 points (10 points for each phase shifter) and more points require significantly increasing experimental time. And thus limited amount of data cannot make the calibration of the cascaded phase shifters sufficiently accurate. When the device is working, there would be thermal crosstalk between neighbour phase shifters and introduces inaccuracies to the target phase of each heating phase shifters, which also reduces the fidelities of experimental data obtained on our device. Other factors like the stability of the classical pump and the polarization maintenance between the chip and superconducting single-photon detectors could also affect the experimental fidelities.

B. Quantum process tomography

Quantum process tomography (QPT) is a well-known approach for experimentally characterizing a quantum operation, which is a complex and resource-intensive procedure providing a complete characterization of the implemented gates in our chip. To perform QPT for each implemented two-qubit gate, we configured 16 separable, linearly independent states $\{\rho_i^{(in)}\} = \{|\psi_i\rangle\langle\psi_i|\}$ as the inputs of the implemented gate, where $|\psi_i\rangle = |\nu_1\rangle \otimes |\nu_2\rangle$ and $\{|\nu_1\rangle, |\nu_2\rangle\} = \{|0\rangle, |1\rangle, |+\rangle = \frac{1}{\sqrt{2}}(|0\rangle + |1\rangle), |+i\rangle = \frac{1}{\sqrt{2}}(|0\rangle + i|1\rangle)\}$. For each input, we measured the output state in a set of 16 basis projections

$$
\begin{aligned}
\{ & |00\rangle\langle 00|, |01\rangle\langle 01|, |0,+\rangle\langle 0,+|, |0,+i\rangle\langle 0,+i|, \\
& |10\rangle\langle 10|, |11\rangle\langle 11|, |1,+\rangle\langle 1,+|, |1,+i\rangle\langle 1,+i|, \\
& |+,0\rangle\langle +,0|, |+,1\rangle\langle +,1|, |+,+\rangle\langle +,+|, |+,+i\rangle\langle +,+i|, \\
& |+i,0\rangle\langle +i,0|, |+i,1\rangle\langle +i,1|, |+i,+\rangle\langle +i,+|, |+i,+i\rangle\langle +i,+i|\},
\end{aligned}
\tag{S57}
$$

and the density matrix of the output state can be experimentally reconstructed via quantum state tomography. On the other hand, the output state can be theoretically obtained as below:

$$
\rho_i^{(out)} = \sum_{m,n=0}^{d^2-1} \chi_{mn} \hat{A}_m \rho_i^{(in)} \hat{A}_n^\dagger \tag{S58}
$$

where $\hat{A}_m$ are the Kraus operators and χ is the corresponding process matrix of the implemented gate. The process matrix χ was reconstructed by using the maximum likelihood techniques, which completely describes the implemented gate. For each implemented gate, QPT requires 256 (=16 × 16) coincidence measurements in total.

The process fidelity was calculated as $F_P = \text{Tr}(\chi_{\text{ideal}}\chi_{\text{exp}})$, where χ_{ideal} and χ_{exp} represent the theoretically ideal and experimentally reconstructed process matrices respectively. The error-bars of process fidelities were estimated by a Monte-Carlo approach assuming Poissonian photon statistics.

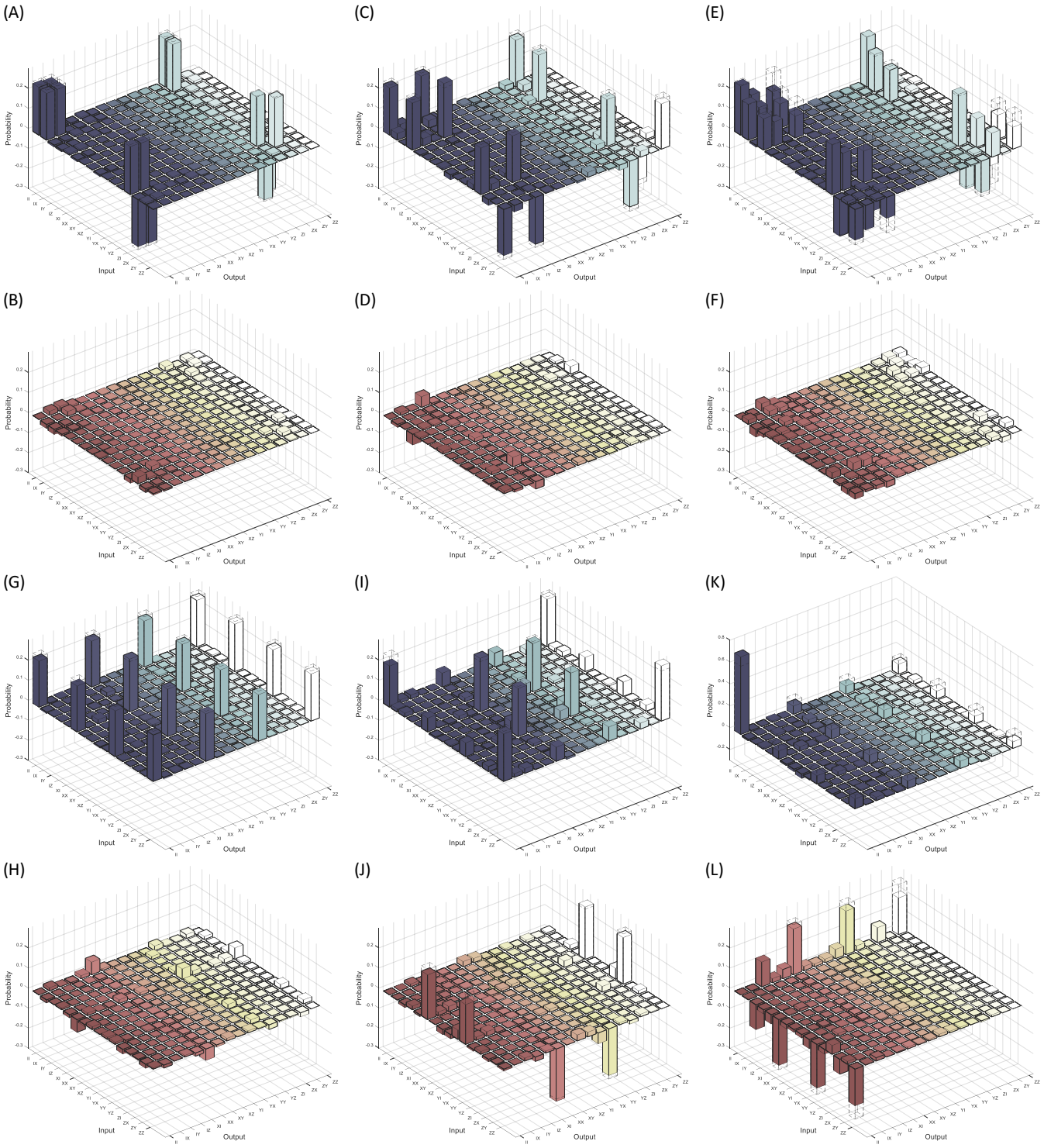

FIG. S9: Experimentally reconstructed process matrices (solid colour) of implemented example quantum logic gates, with theoretical prediction represented by overlaid empty frames. (A, B) The real and imaginary parts of the process matrix of CNOT. (C, D) The real and imaginary parts of the process matrix of CZ. (E, F) The real and imaginary parts of the process matrix of CH. (G, H) The real and imaginary parts of the process matrix of SWAP. (I, J) The real and imaginary parts of the process matrix of iSWAP. (K, L) The real and imaginary parts of the process matrix of $\sqrt{\text{SWAP}}$.

C. Demonstrating QAOA

Here we present more details of applying QAOA for the three example CSPs shown in the main text. The objective function of CSP_1 is

$$C(z) = \tfrac{1}{2} + \tfrac{1}{2} z_1 z_2. \tag{S59}$$

According to QAOA process, the two operators with angles γ and δ are obtained as below:

$$e^{-i\gamma C} = e^{-i\gamma[\frac{1}{2} + \frac{1}{2} Z_1 Z_2]} = e^{-i\gamma\frac{1}{2}} e^{-i\gamma Z_1 Z_2} \tag{S60}$$

$$e^{-i\beta B} = e^{-i\beta(X_1 + X_2)} \tag{S61}$$

where X and Z represent Pauli operators σ_x and σ_z respectively. The $|\gamma, \beta\rangle_{\mathrm{CSP}_1}$ state is obtained as

$$\begin{aligned} |\gamma, \beta\rangle_{\mathrm{CSP}_1} &= e^{-i\beta B} e^{-i\gamma C} H \otimes H \,|00\rangle \\ &= e^{-i\gamma\frac{1}{2}} e^{-i\beta X_1} e^{-i\beta X_2} e^{-i\gamma\frac{1}{2} Z_1 Z_2} H \otimes H \,|00\rangle \,. \end{aligned} \tag{S62}$$

It is easy to verify that for CSP_1 two strings of z: $\{1, 1\}$ and $\{-1, -1\}$ can satisfy the only constraint and make $C(z) = 1$.

The objective function of CSP_2 is

$$C(z) = \left(\tfrac{1}{2} + \tfrac{1}{2} z_1\right) + \left(\tfrac{1}{2} + \tfrac{1}{2} z_2\right) + \left(\tfrac{1}{2} + \tfrac{1}{2} z_1 z_2\right) \tag{S63}$$

and similarly the $|\gamma, \beta\rangle_{\mathrm{CSP}_2}$ state is obtained as

$$\begin{aligned} |\gamma, \beta\rangle_{\mathrm{CSP}_2} &= e^{-i\beta B} e^{-i\gamma C} H \otimes H \,|00\rangle \\ &= e^{-i\gamma\frac{3}{2}} e^{-i\beta X_1} e^{-i\beta X_2} e^{-i\gamma\frac{1}{2}(Z_1 + Z_2 + Z_1 Z_2)} H \otimes H \,|00\rangle \,. \end{aligned} \tag{S64}$$

For the strings $z = \{1, 1\}, \{1, -1\}, \{-1, 1\}, \{-1, -1\}$, the values of C are 3, 1, 1, -1 respectively. Therefore, the string $z = \{1, 1\}$ is the target string, and as we showed in the main text, the $p = 1$ QAOA outputs $\{z_1, z_2\} = \{1, 1\}$ with highest probability.

The objective function of CSP_3 is

$$C(z) = \left(\tfrac{1}{2} + \tfrac{1}{2} z_1\right) + \left(\tfrac{1}{2} + \tfrac{1}{2} z_2\right) + \left(\tfrac{1}{2} - \tfrac{1}{2} z_1 z_2\right) \tag{S65}$$

and the $|\gamma, \beta\rangle_{\mathrm{CSP}_3}$ state is obtained as

$$\begin{aligned} |\gamma, \beta\rangle_{\mathrm{CSP}_3} &= e^{-i\beta B} e^{-i\gamma C} H \otimes H \,|00\rangle \\ &= e^{-i\gamma\frac{3}{2}} e^{-i\beta X_1} e^{-i\beta X_2} e^{-i\gamma\frac{1}{2}(Z_1 + Z_2 - Z_1 Z_2)} H \otimes H \,|00\rangle \,. \end{aligned} \tag{S66}$$

For the strings $z = \{1, 1\}, \{1, -1\}, \{-1, 1\}, \{-1, -1\}$, the values of C are 1, 1, 1, -3 respectively. Therefore, there are three strings all can maximize the object function C of CSP_3. With proper γ and β, the $p = 1$ QAOA outputs the measurement result as $\{z_1, z_2\} = \{1, 1\}, \{1, -1\}, \{-1, 1\}$ with approximate probability of 1/3 each.

Quantum circuits that implement QAOA for the three example CSPs (Fig. 3(A) in the main text) use only one two-qubit entangling gate, and thus they can be implemented using half capability of our chip. The typical integration time for a single measurement of $|\gamma, \beta\rangle$ with each pair of $\{\gamma, \beta\}$ is 15 seconds in our experiment, and the total cost time of experimentally obtaining $\langle\gamma, \beta|C|\gamma, \beta\rangle$ for all 600 pairs of $|\gamma, \beta\rangle$ is more than 10 hours.

D. Simulating Szegedy quantum walk

The periodicity of SQW can be theoretically analyzed by using spectral decomposition of the single-step evolution operator U_{sz}. U_{sz} can be decomposed into the following form:

$$U_{\mathrm{sz}} = \sum_{i=1}^{N^2} \lambda_i \,|i\rangle \langle i| \,, \tag{S67}$$

where λ_i and $|i\rangle$ are eigenvalues and corresponding eigenvectors. A general initial state $|\psi\rangle$ for SQW is given by

$$|\psi\rangle = \sum_{i=1}^{N^2} \alpha_i |i\rangle , \tag{S68}$$

where α_i satisfy that $\sum_{i=1}^{N^2} |\alpha_i|^2 = 1$. The evolution state of a single step of SQW is obtained as

$$U_{\rm sz} |\psi\rangle = \sum_{i=1}^{N^2} \lambda_i \alpha_i |i\rangle , \tag{S69}$$

and the evolution state of SQW of t steps is determined by

$$(U_{\rm sz})^t |\psi\rangle = \sum_{i=1}^{N^2} \lambda_i^t \alpha_i |i\rangle . \tag{S70}$$

Given that $U_{\rm sz}$ is unitary, for all eigenvalues λ_i of $U_{\rm sz}$, $|\lambda_i| = 1$. An eigenvalue is said to be a root of unity if there exists a natural number n such that $\lambda^n = 1$, where n is the period. The single-step evolution operator $U_{\rm sz}$ is periodic if and only if all its corresponding eigenvalues are roots of unity with a common period. If $U_{\rm sz}$ is periodic, its period is given by the lowest common multiple of the periods of its eigenvalues. Using this analysis it was found that SQWs on the given two-node complete graph are periodic for the cases $\alpha = \beta = \frac{1}{4}$, $\frac{1}{2}$, $\frac{3}{4}$ and 1 with periods of 6, 4, 6 and 2 steps respectively. Moreover, SQWs are periodic for the cases $\alpha + \beta = 1$ and $\alpha + \beta = \frac{1}{2}$ with periods of 4 and 6 steps respectively.

In our experiments, we implemented SQWs for various cases of weights α and β with three different initial states: $|0\rangle|0\rangle$, $\frac{1}{\sqrt{2}}|0\rangle(|0\rangle + |1\rangle)$ and $\frac{1}{\sqrt{2}}|0\rangle(|0\rangle + i|1\rangle)$. For each case, we realized the first 200 steps of SQW and measured the probability of the walker being at node 1 at each step. We calculated the average fidelities of the obtained probability distributions, as listed in Table. II. It is worth noting that SQWs on the example two-node graph do not have perfect periodicity for general symmetric weights, however, the obtained probability distributions may show quasi periodic behaviors for some specific cases. As shown in Figure. S10, SQWs for the cases $\alpha = \beta = 0.43, 0.45, 0.47$ show quasi-periodicities. This could be useful for designing SQW-based quantum algorithms.

TABLE II: Experimental results of SQWs on the example two-node graphs.

$\{\alpha, \beta\}$	**Initial state**	**Step number**	**Average fidelity**
$\{0.1, 0.9\}$	$\|0\rangle\|0\rangle$	200	98.35±0.15%
	$\frac{1}{\sqrt{2}}\|0\rangle(\|0\rangle + \|1\rangle)$	200	99.38±0.03%
	$\frac{1}{\sqrt{2}}\|0\rangle(\|0\rangle + i\|1\rangle)$	200	99.13±0.04%
$\{0.3, 0.7\}$	$\|0\rangle\|0\rangle$	200	97.99±0.10%
	$\frac{1}{\sqrt{2}}\|0\rangle(\|0\rangle + \|1\rangle)$	200	99.31±0.04%
	$\frac{1}{\sqrt{2}}\|0\rangle(\|0\rangle + i\|1\rangle)$	200	98.71±0.05%
$\{0.25, 0.25\}$	$\|0\rangle\|0\rangle$	200	98.46±0.04%
	$\frac{1}{\sqrt{2}}\|0\rangle(\|0\rangle + \|1\rangle)$	200	99.28±0.02%
	$\frac{1}{\sqrt{2}}\|0\rangle(\|0\rangle + i\|1\rangle)$	200	98.71±0.05%
$\{0.5, 0.5\}$	$\|0\rangle\|0\rangle$	200	98.48±0.04%
	$\frac{1}{\sqrt{2}}\|0\rangle(\|0\rangle + \|1\rangle)$	200	99.02±0.11%
	$\frac{1}{\sqrt{2}}\|0\rangle(\|0\rangle + i\|1\rangle)$	200	98.81±0.03%
$\{0.43, 0.43\}$	$\|0\rangle\|0\rangle$	200	98.02±0.04%
	$\frac{1}{\sqrt{2}}\|0\rangle(\|0\rangle + \|1\rangle)$	200	99.23±0.02%
	$\frac{1}{\sqrt{2}}\|0\rangle(\|0\rangle + i\|1\rangle)$	200	98.88±0.03%
$\{0.45, 0.45\}$	$\|0\rangle\|0\rangle$	200	97.86±0.04%
	$\frac{1}{\sqrt{2}}\|0\rangle(\|0\rangle + \|1\rangle)$	200	99.12±0.04%
	$\frac{1}{\sqrt{2}}\|0\rangle(\|0\rangle + i\|1\rangle)$	200	98.75±0.03%
$\{0.47, 0.47\}$	$\|0\rangle\|0\rangle$	200	98.11±0.04%
	$\frac{1}{\sqrt{2}}\|0\rangle(\|0\rangle + \|1\rangle)$	200	99.30±0.02%
	$\frac{1}{\sqrt{2}}\|0\rangle(\|0\rangle + i\|1\rangle)$	200	98.84±0.03%

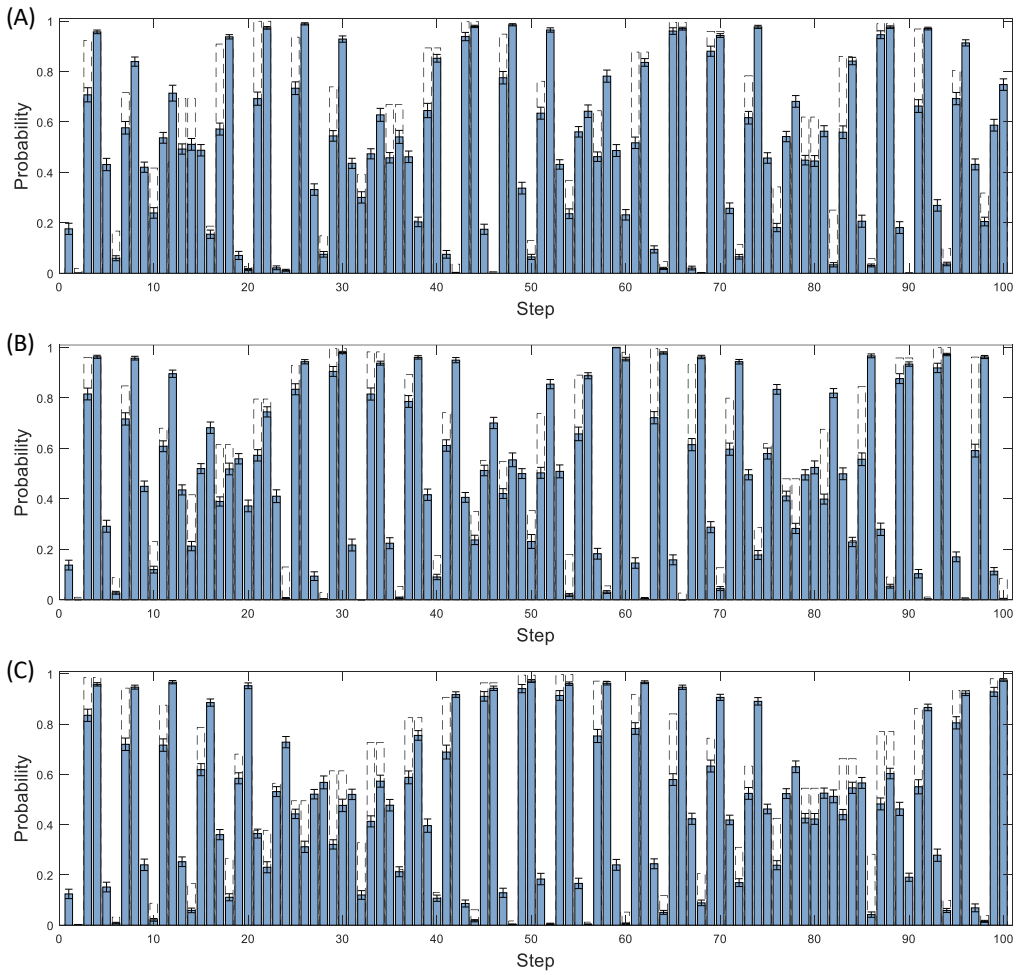

FIG. S10: Experimental obtained probability distributions of SQWs with the theoretical distribution overlaid. (A) Probability distribution (of the walker being at node 1) of the first 100 steps of SQW on the example two-node graph with $\alpha = \beta = 0.43$ and an initial state of $|00\rangle$. (B) Probability distribution (of the walker being at node 1) of the first 100 steps of SQW on the example two-node graph with $\alpha = \beta = 0.45$ and an initial state of $|00\rangle$. (C) Probability distribution (of the walker being at node 1) of the first 100 steps of SQW on the example two-node graph with $\alpha = \beta = 0.47$ and an initial state of $|00\rangle$. The s.d. of each individual probability is calculated by propagating error assuming Poissonian statistics.

* Electronic address: zhouxq8@mail.sysu.edu.cn
† Electronic address: jonathan.matthews@bristol.ac.uk

[1] Navin Khaneja and Steffen J Glaser. Cartan decomposition of su (2n) and control of spin systems. *Chemical Physics*, 267(1):11–23, 2001.
[2] Robert R Tucci. An introduction to cartan's kak decomposition for qc programmers. *arXiv preprint quant-ph/0507171*, 2005.
[3] Michael A Nielsen and Isaac L Chuang. *Quantum computation and quantum information*. Cambridge university press, 2010.
[4] Jianwei Wang, Stefano Paesani, Yunhong Ding, Raffaele Santagati, Paul Skrzypczyk, Alexia Salavrakos, Jordi Tura, Remigiusz Augusiak, Laura Mančinska, Davide Bacco, et al. Multidimensional quantum entanglement with large-scale integrated optics. *Science*, page eaar7053, 2018.
[5] Guifre Vidal and Christopher M Dawson. Universal quantum circuit for two-qubit transformations with three controlled-not gates. *Physical Review A*, 69(1):010301, 2004.
[6] Jeremy L O'Brien, Akira Furusawa, and Jelena Vučković. Photonic quantum technologies. *Nature Photonics*, 3(12):687–695, 2009.
[7] Emanuel Knill, Raymond Laflamme, and Gerald J Milburn. A scheme for efficient quantum computation with linear optics. *Nature*, 409(6816):46–52, 2001.

[8] TB Pittman, BC Jacobs, and JD Franson. Probabilistic quantum logic operations using polarizing beam splitters. *Physical Review A*, 64(6):062311, 2001.

[9] Holger F Hofmann and Shigeki Takeuchi. Quantum phase gate for photonic qubits using only beam splitters and postselection. *Physical Review A*, 66(2):024308, 2002.

[10] Timothy C Ralph, Nathan K Langford, TB Bell, and AG White. Linear optical controlled-not gate in the coincidence basis. *Physical Review A*, 65(6):062324, 2002.

[11] Robert Raussendorf and Hans J Briegel. A one-way quantum computer. *Physical Review Letters*, 86(22):5188, 2001.

[12] Stefanie Barz. Quantum computing with photons: introduction to the circuit model, the one-way quantum computer, and the fundamental principles of photonic experiments. *Journal of Physics B: Atomic, Molecular and Optical Physics*, 48(8):083001, 2015.

[13] Nikolai Kiesel, Christian Schmid, Ulrich Weber, Géza Tóth, Otfried Gühne, Rupert Ursin, and Harald Weinfurter. Experimental analysis of a four-qubit photon cluster state. *Physical Review Letters*, 95(21):210502, 2005.

[14] Robert Prevedel, Philip Walther, Felix Tiefenbacher, Pascal Böhi, Rainer Kaltenbaek, Thomas Jennewein, and Anton Zeilinger. High-speed linear optics quantum computing using active feed-forward. *Nature*, 445(7123):65–69, 2007.

[15] Stefanie Barz, Elham Kashefi, Anne Broadbent, Joseph F Fitzsimons, Anton Zeilinger, and Philip Walther. Demonstration of blind quantum computing. *Science*, 335(6066):303–308, 2012.

[16] Daniel E Browne and Terry Rudolph. Resource-efficient linear optical quantum computation. *Physical Review Letters*, 95(1):010501, 2005.

[17] Michael Reck, Anton Zeilinger, Herbert J Bernstein, and Philip Bertani. Experimental realization of any discrete unitary operator. *Physical review letters*, 73(1):58, 1994.

[18] Jacques Carolan, Christopher Harrold, Chris Sparrow, Enrique Martín-López, Nicholas J Russell, Joshua W Silverstone, Peter J Shadbolt, Nobuyuki Matsuda, Manabu Oguma, Mikitaka Itoh, et al. Universal linear optics. *Science*, 349(6249):711–716, 2015.

[19] R. Strek, M. Miuda, M. Mikov, I. Straka, M. Duek, M. Jeek, and J. Fiurek. Experimental investigation of a four-qubit linear-optical quantum logic circuit. *Scientific Reports*, 6:33475, September 2016.

[20] Callum M. Wilkes, Xiaogang Qiang, Jianwei Wang, Raffaele Santagati, Stefano Paesani, Xiaoqi Zhou, David A. B. Miller, Graham D. Marshall, Mark G. Thompson, and Jeremy L. O'Brien. 60db high-extinction auto-configured mach–zehnder interferometer. *Optics Letters*, 41:5318–5321, 2016.